J. Fluid Mech. (1989), *vol.* 203, *pp.* 557–575
Printed in Great Britain

Flow past short circular cylinders with two free ends

By M. M. ZDRAVKOVICH, V. P. BRAND, G. MATHEW† AND A. WESTON

Department of Aeronautical and Mechanical Engineering, University of Salford, Salford M5 4WT, UK

(Received 3 April 1987 and in revised form 10 January 1989)

Preliminary tests have been carried out on short circular cylinders with both ends free. Drag force is measured across the range $6 \times 10^4 < Re < 2.6 \times 10^5$ for cylinders of length to diameter ratio L/D between 1 and 10. The effect of hemispherical ends is also investigated. A kind of periodic vortex shedding is found in the range $2 < L/D < 8$. The oil-film surface flow visualization shows that the 'eyes' near the free ends (regions of low pressure) gradually disappear as L/D is reduced to 3. An asymmetric flow pattern is established for very short cylinders ($L/D < 3$). The detailed measurements of pressure distribution along and across models shows asymmetries of minimum and base pressures along the span. The asymmetric flow produces yawing and rolling moments which are also measured.

1. Introduction

Flow around a *nominally* two-dimensional circular cylinder in the disturbance-free stream has attracted an enormous amount of research (Zdravkovich 1988). However, in most practical applications there is at least one free end (chimney stacks, gas and oil storage reservoirs, etc), and sometimes two free ends (ship radar aerials, submerged vehicles, fibres, projectiles carried by a tornado, etc). The latter has attracted the least attention so far.

When a cantilevered cylinder has a finite length, the height-to-diameter ratio, H/D becomes an influencing parameter. Etzold & Fielder (1976) found that the near wake underwent a structural change in the range $5 \leqslant H/D \leqslant 6$ when the free stream was uniform:

(i) For $H/D > 6$, alternate vortex shedding occurred along most of the span except near the free end. The interaction of the vortex shedding and the free end was extremely complex as shown by the flow visualization carried out by Taneda (1952), Gould, Raymer & Ponsford (1968), Okamoto & Yagita (1973), Etzold & Fiedler (1976), Slaouti & Gerrard (1981) and Kawamura *et al.* (1984*a*, *b*). Distinct 'eyes' on the surface near the free end are displayed by the oil-film visualization seen in figure 1 (after Gould *et al.* 1968). The 'eye' was associated with low pressure which increased the local drag coefficient, see Gould *et al.* (1968). A similar finding was made by Farivar (1981) who reported two different frequencies of vortex shedding near the free end for $H/D > 6$.

(ii) For $H/D = 5$, Gould *et al.* (1968) reported in-phase pressure fluctuations on two sides of the cylinder. Sakamoto & Arie (1983) photographed the arch-shaped vortices formed behind a short cylinder submerged in a thick boundary layer,

† Present address: Arthur Andersen & Co., The Information Consultancy, Chicago, Illinois, USA.

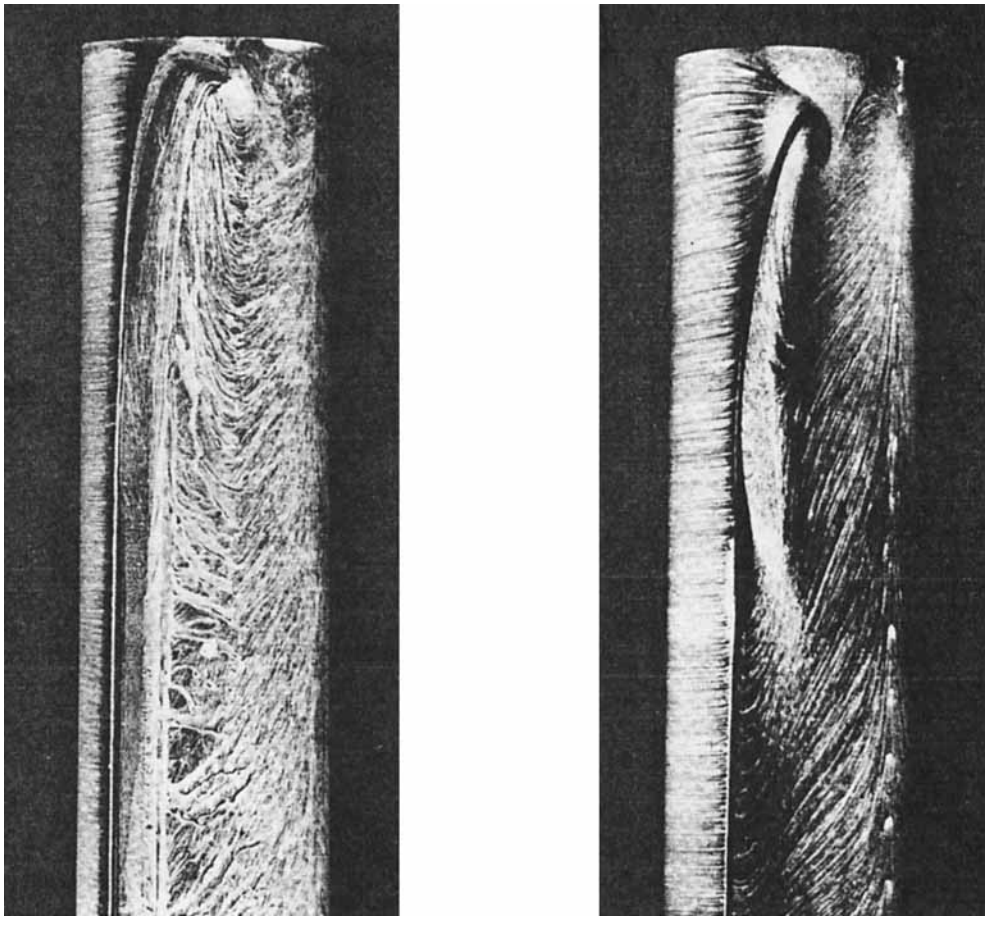

Low Reynolds number, zero efflux

High Reynolds number, zero efflux

FIGURE 1. Oil-film patterns near an open free end; Gould *et al.* (1968).

$0.5 < \delta/H < 1$, where δ is the boundary-layer thickness. The change-over from an alternate to a symmetric vortex street occurred for $H/D < 2.5$. This was in variance with $H/D = 5$ found by Gould *et al.* (1968); presumably owing to the thick turbulent boundary layer.

The earliest reported tests on finite cylinders with two free ends were by Wieselsberger (1922). He measured the variation of drag coefficient with a length-to-diameter ratio from 1 to 10 and also the variation of drag coefficient for $L/D = 5$ in the range $400 < Re < 8 \times 10^5$. Here, L is the length of the cylinder and $Re = VD/\nu$ the Reynolds number where V is the free-stream velocity and ν the kinematic viscosity. Further tests have not been reported in the open literature until recently.

The present investigation was motivated by both the fundamental and applied side of the problem: (i) The short cylinder with two free ends has two interacting side flows which may inhibit the vortex shedding. (ii) The short cylinder with two hemispherical ends is the shape of an underwater remotely operated vehicle (ROV). The positioning of the ROV in a strong current requires knowledge of hydrodynamic forces, and control depends on a minimum drag in the side position.

2. Experimental arrangement

The wind tunnel used had a closed working section, closed circuit, and was capable of continuous variation of velocity in the range of 15 m/s to 35 m/s. The working section dimensions were 1.2 m (width) by 0.91 m (height). After passing the 5:1 contraction section, the free-stream longitudinal turbulence intensity in the empty working section was 0.3%.

A six-component balance was situated immediately above the working section. The major part of the model weight was supported by two fixed vertical struts which protruded into the working section, shielded from the flow by streamlined shrouds. A third arm downstream from the first two recorded the pitching moment on the model. Models were 'sting' mounted upstream of the main struts on a light aluminium frame as shown in figure 2. The six-component balance was capable of measuring all three forces and three moments by using a set of load cells. Signals from all these gauges were transmitted into a 'solatron' programmer from which the signals of interest to the experiment might be directed to a teletype printer. In this investigation the drag force, rolling and yawing moments were measured.

An oil-film technique was employed for surface flow visualization. A mixture of fluorescent powder, paraffin and light oil was applied using a brush along the cylinder axis. After exposing the cylinder to the air flow for about 10 min at the maximum wind tunnel speed ($Re = 1.4 \times 10^5$), the resulting powder patterns were photographed under an ultraviolet light.

Models used were modified a number of times during the investigation. The models of a circular cylinder with two flat ends for drag measurements and flow visualization were made of PVC tubing of 50 mm, 68 mm and 89 mm outer diameters. The length-to-diameter ratios were 2, 4, 5, 6, 8 and 10. All the models were attached to the balance in the same way, using the light aluminium cross-frame section shown in figure 2.

Pressure distributions were measured on specially designed models. The basic cylindrical model was 127 mm (5 in.) in diameter and could be fitted with either flat or hemispherical end caps (see figure 3). This size was chosen as an optimum for drag force and blockage. High drag forces were desired for small-length-to diameter ratios, whilst the model was to have a low blockage effect. The actual blockage was only 1.36% and 2.73% for flat-ended models having $L/D = 1$ and 2, respectively, and is possibly reduced by a perforated ceiling of the test section (see figure 3). The models were subsequently adapted to allow for length-to-diameter ratio values of 2, 2.5 and 3 with hemispherical end caps. Four 'spacers' were made, with spiggots to allow simple variation of length-to-diameter ratio.

The vortex shedding frequency was measured by using a single hot wire, DISA constant-temperature anemometer and a Bruel and Kjaer frequency analyser. The optimal position of the hot wire was found to be at $x/D = 1.7$, $y/D = 0.7$, and $z/D = 0$, where x is in the direction along the free stream and midway between the free ends, y is normal to the free stream and cylinder axis and z is along the cylinder axis. The signal was displayed on an oscilloscope screen for simultaneous visual observation.

3. Drag force measurements

The measured drag force was reduced to a drag coefficient C_D by dividing drag F by the free-stream dynamic pressure q_0 and the area, taken to be length times

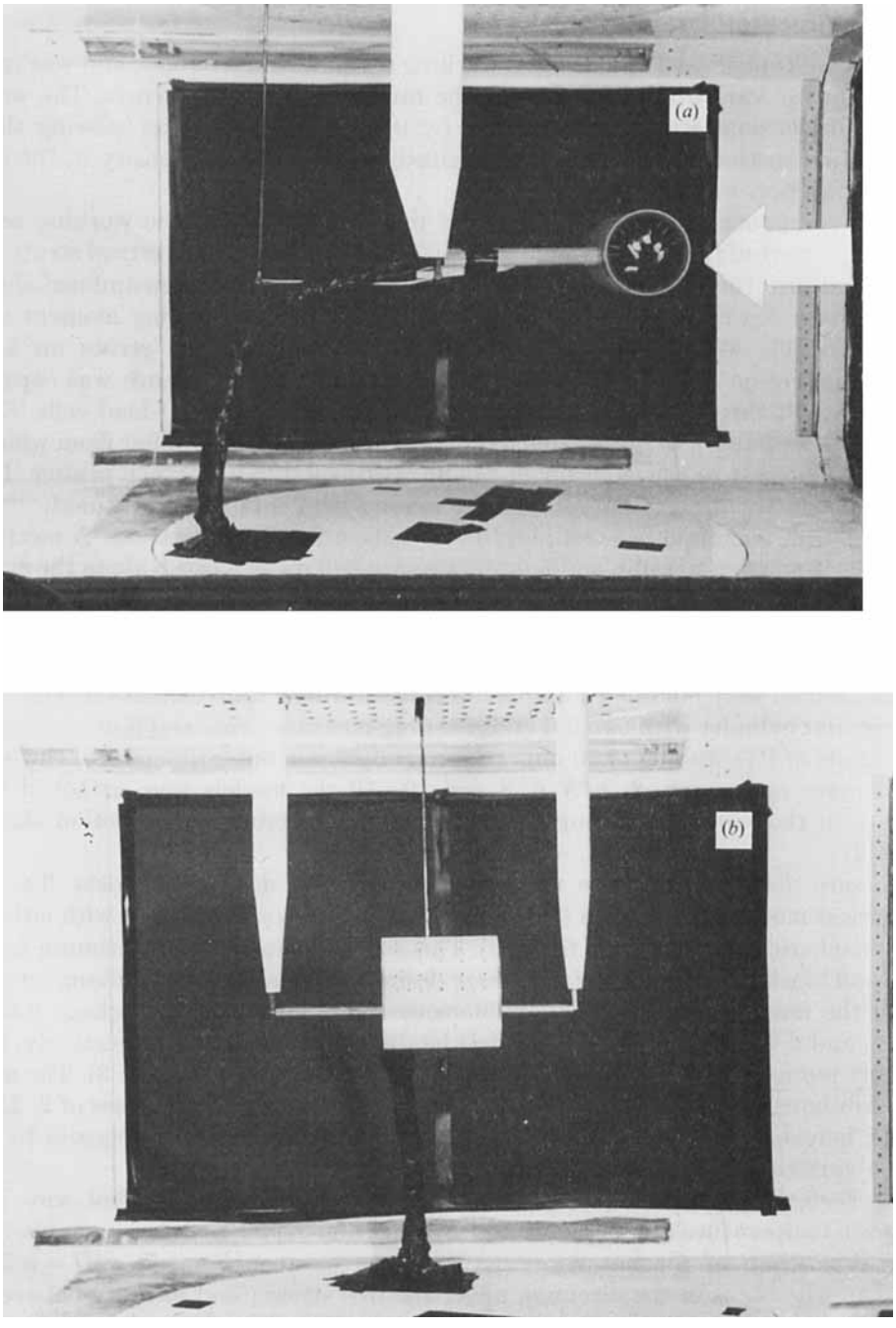

FIGURE 2. Model support in test section: (*a*) side view, (*b*) front view.

diameter of the cylinder. The free-stream velocity was expressed by the Reynolds number based on the cylinder diameter, see §1.

Figure 4 shows the drag coefficient C_D in terms of Reynolds number for various length-to-diameter ratios L/D. Wieselsberger's (1922) curve for $L/D = 5$ is partly reproduced in the range $6 \times 10^4 < Re < 2.6 \times 10^5$, i.e. without a discontinuous drop of

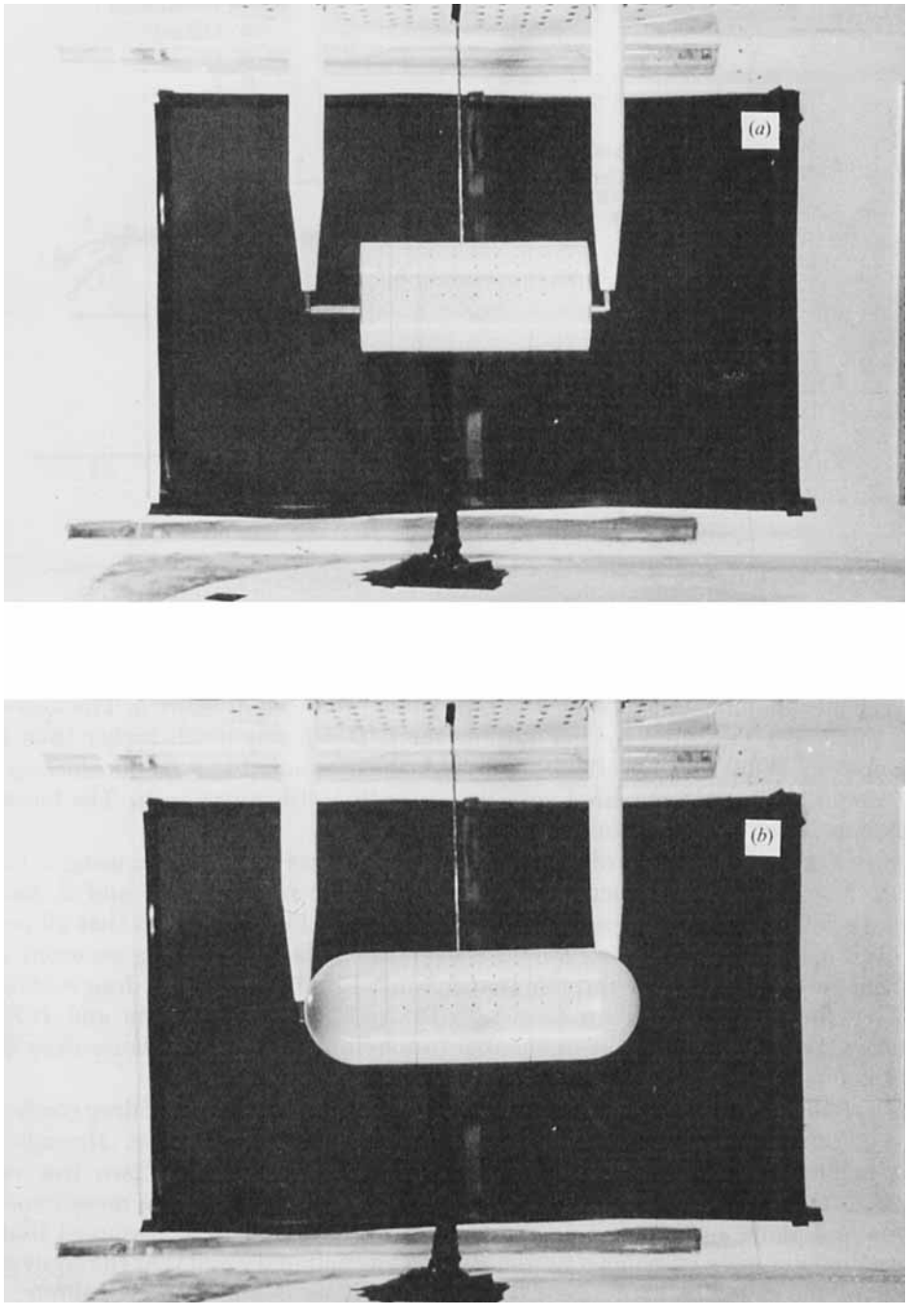

FIGURE 3. Models for pressure measurements: (*a*) flat ends, (*b*) hemispherical ends.

drag coefficient to 0.3 at 4.5×10^5 owing to the formation of separation bubbles. The present measurements with a 68 mm diameter cylinder are limited to $Re = 1.6 \times 10^5$, the top speed of the wind tunnel. The experimental points exhibit a considerable scatter in spite of the fact that each point represents a mean value of twelve readings

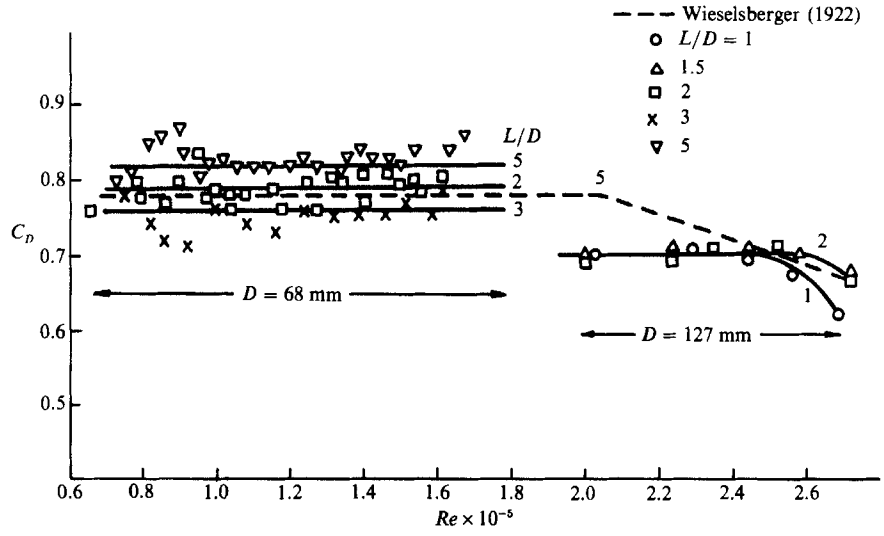

FIGURE 4. Drag coefficient variation with Reynolds number and L/D.

during a 2 min run. The source of scatter could not be traced to either the resonance of the model or to the electronic devices and seemed to be a genuine feature of the measured forces. Further averaging is done by drawing straight lines between the experimental points, and these values only are reproduced in figure 5. The averaged drag coefficient measured by the authors for $L/D = 5$ was much higher than that measured by Wieselsberger (1922); this might be attributed to a larger blockage for the present tests, 2% compared with 0.8% for Wieselsberger's tests. The blockage correction is not available for short cylinders.

Considerably less scatter of experimental points was found when using a larger model, $D = 127$ mm, and smaller length-to-diameter ratios, 1, 1.5 and 2, having blockage ratios 1.36%, 2.05 and 2.73%, respectively. Figure 4 shows that all points fell onto a single curve up to $Re = 2.4 \times 10^5$ when the fall in drag occurred at a different rate. It came as a surprise that a kind of step-like drop in drag coefficient occurred for $L/D = 2$ between $Re = 1.6 \times 10^5$ and 2×10^5 for 68 mm and 127 mm cylinders, respectively. It was impossible to overlap the results because drag force could not be measured below 2×10^5 for the 127 mm cylinder.

Wieselsberger (1922) also systematically measured the variation of drag coefficient with length-to-diameter ratio. Figure 5 shows a full-line drawn through his experimental points obtained by using a 80 mm cylinder with two free ends. Okamoto & Yagita (1973) evaluated drag coefficients from pressure measurements around and along a cantilevered cylinder with one free end. They assumed that an equivalent cylinder was symmetric about the plane boundary and that the equivalent length of the cylinder with two free ends should be doubled. For example, if a cantilevered cylinder on the boundary has $H/D = 5$ then the equivalent cylinder with two free ends should have $L/D = 10$. Figure 5 shows that their experimental points are below Wieselsberger's (1922) curve.

Recently, D. J. Maull (1987, private communication) and his students measured drag on cylinders with two free ends ($L/D = 3.75$, 5, 6.25 and 7.5) in the range of $3 \times 10^4 < Re < 2.4 \times 10^5$. Only drag coefficients measured at $Re = 8.8 \times 10^4$ are shown in figure 5. They are all above Wieselsberger's (1922) curve, as are the present

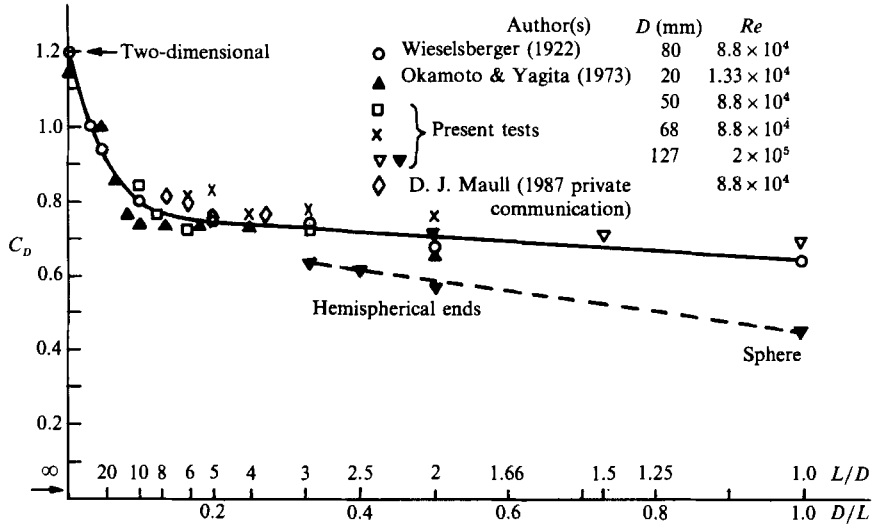

FIGURE 5. Drag coefficient variation with L/D and Re.

measurements with three sizes of cylinders. The drag coefficient of the cylinders with hemispherical ends will be discussed in the next section.

4. Discussion of flow structures

An inevitable question arises: why does the reduction of the length-to-diameter ratio continually decrease the drag coefficient?

Muttray (1932) offered a simple physical argument: 'The explanation for the fall of drag coefficient with decreasing aspect ratio should be sought in the venting of a near wake† behind a bluff body, i.e. an inflow of the fluid into the near wake space on its way around the cylinder ends. Hence the pressure over the back side of the body would rise and so the drag would be smaller'.

This correct physical argument needs three minor additions for updating:

(i) The 'inflow' consists of fluid near the (x, z)-plane of symmetry that flows around the free ends, as depicted in figure 6. It takes some time for the inflow to turn and reach the near wake. The result is a low-pressure region near the free ends causing a high local drag coefficient as found by Gould *et al.* (1968).

(ii) The separated shear layers from the sharp-edged circular ends form two counter-rotating swirling vortices, shown in figure 6, like those formed along the leading edge of the delta wing at an angle of incidence. The swirling vortices separate from the free ends where the flow around the rest of the cylinder does and are carried downstream as a streamwise vortex pair, the chain-dotted lines sketched in figure 6. The strength of swirling vortices is enhanced further downstream by the inflow along the (x, z)-plane.

(iii) The effect of the inflow on the near wake along the span does not merely increase the base pressure, as inferred correctly by Wieselsberger (1922), but also displaces the vortex formation region further downstream, as found by Etzold & Fieldler (1976) and widens the separated shear layers before roll-up into vortices. The former contributes additionally to the reduction of drag coefficient and the latter

† The original German word 'deadwater' is updated with 'near wake'.

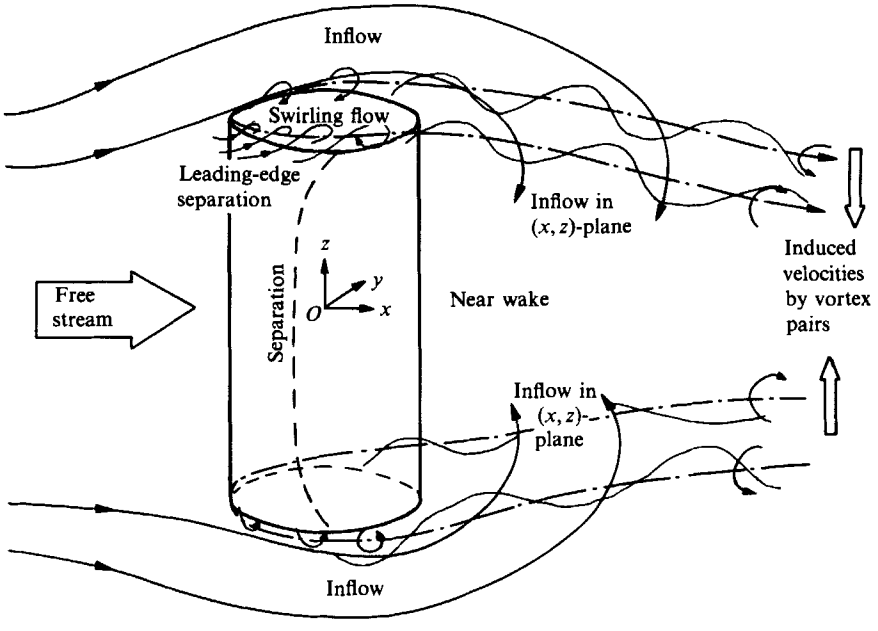

FIGURE 6. Sketch of flow around free ends.

causes the decrease of frequency of vortex shedding. The Strouhal number measured behind finite cylinders was always smaller than behind the infinite cylinder, see Okamoto & Yagita (1973), Farivar (1981) and Ayoub & Karamcheti (1982).

Let us apply these qualitative physical arguments to explain the quantitative variation of drag coefficient with the length-to-diameter ratio shown in figure 5. The rapid rate of fall of drag coefficient corresponds to an effective venting of the near wake, i.e. intensive inflow. For example for $L/D = 10$, the drag coefficient is reduced 31% in comparison to the drag coefficient of a cylinder of infinite span.

There is a smaller reduction of the rate of fall of drag coefficient with further shortening of the cylinder down to $L/D = 6$. For example, the drag coefficient is reduced by another 6% in comparison to the $L/D = 10$. For shorter cylinders, $1 < L/D < 6$, there is a very small rate of change of drag coefficient and the curve in figure 5 appears almost as a horizontal line; this indicates that further inflow is restricted by the sharp flat ends.

Muttray (1932) compared the drag of a sphere $D/D = 1$ and cylinder $L/D = 1$ and noted that they are in the ratio 1 : 1.4, respectively. The additional 40% drag of the short circular cylinder measured by Wieselsberger (1922) was attributed to the 'edge' drag, i.e. the sharp edges of the flat ends producing wider separation than the sphere.

The sphere may be thought of as a special case of the circular cylinder with hemispherical ends having $L/D = 1$. The broken curve in figure 5 shows the average values of the drag coefficient measured on circular cylinders fitted with hemispherical ends. The three short cylinders with hemispherical ends produce significantly lower drag than the same cylinders with flat ends (19% fall for $L/D = 2$). This shows convincingly that for short cylinders, say $L/D < 5$, the shape of the free end becomes a governing factor. Note that, unlike the sphere, L/D of the cylinder can be reduced down to zero when, presumably, the drag coefficient tends to zero.

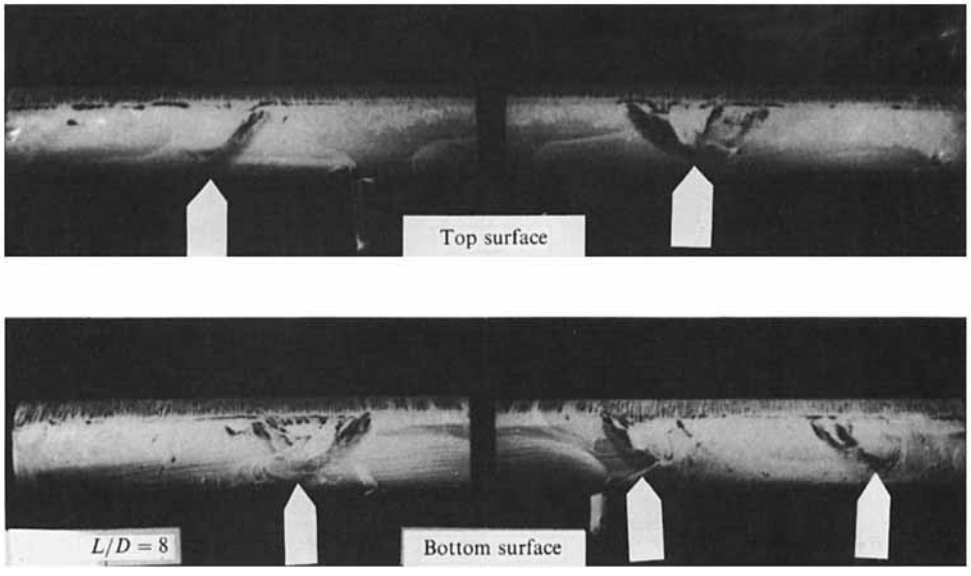

FIGURE 7. Surface oil-film pattern for $L/D = 8$ (four separate records).

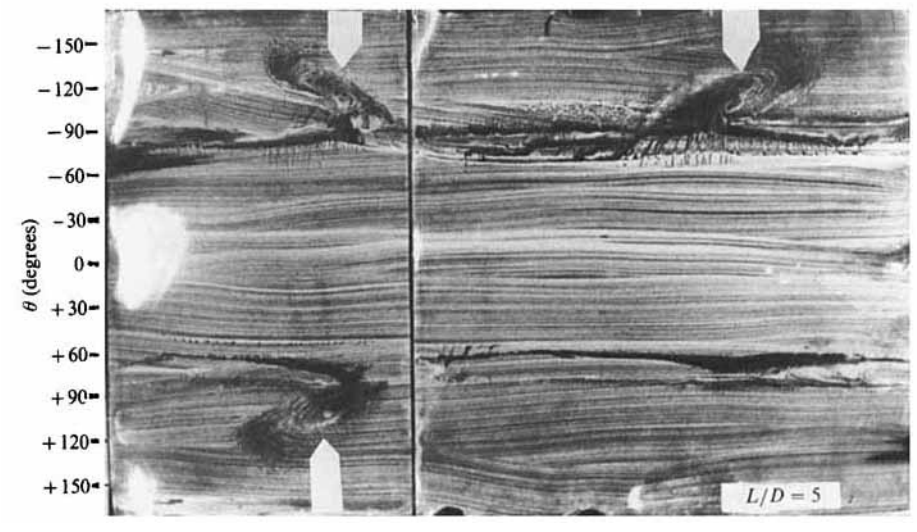

FIGURE 8. Surface oil-film pattern for $L/D = 5$ (two separate records).

5. Surface flow visualization

Gould *et al.* (1968) have shown by using surface flow visualization that there was a prominent eye-like pattern near the *open* free end caused by the swirling secondary flow behind the separation lines. They found that the attachment of the swirling vortex on the rear side of the cantilevered $H/D = 12$ cylinder was at $\pm 145°$ and 0.3 diameters from the open free end. The distinct eye-like patterns were also observed behind the upstream cylinder of two cylinders forming a cross as reported by Zdravkovich (1983). The object of the present surface flow visualization was to

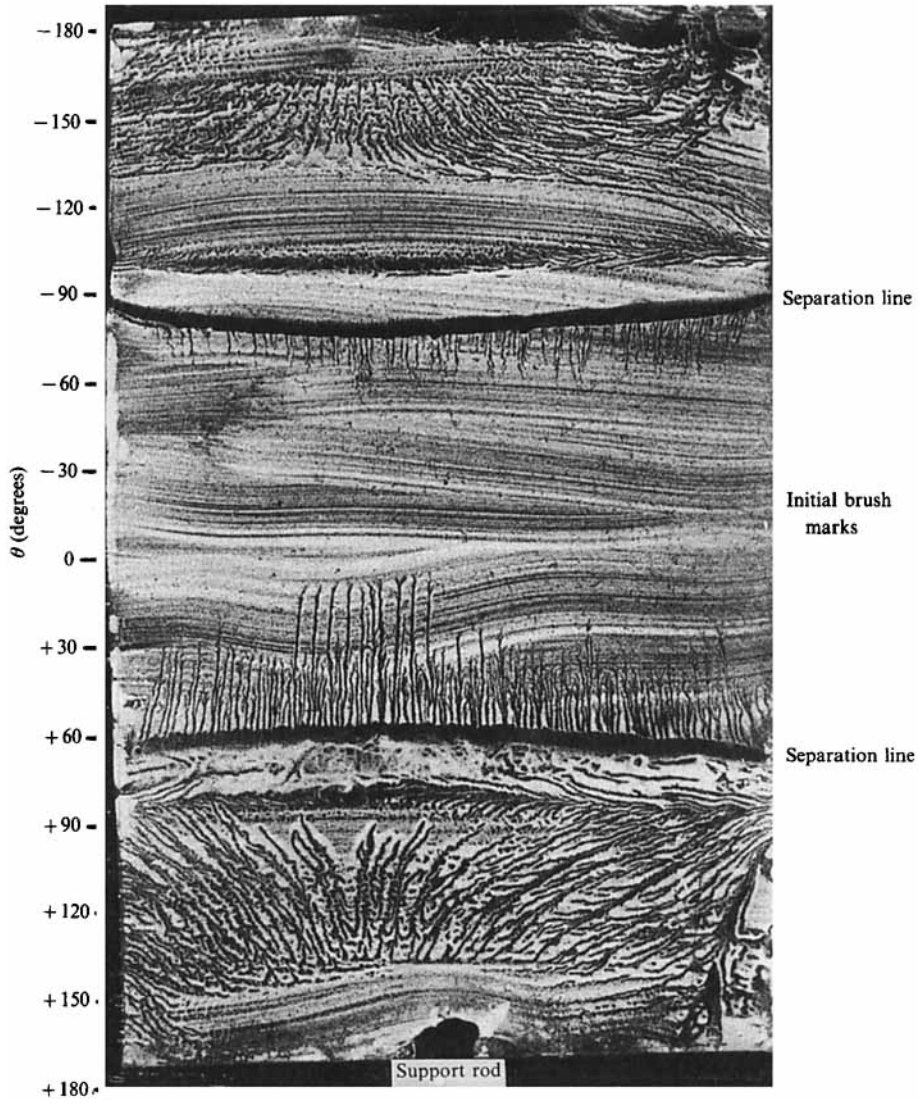

FIGURE 9. Surface oil-film pattern for $L/D = 2$ (single record).

repeat surface flow visualization for cylinders with two *closed* free ends and to examine the effect of shortening the cylinder, i.e. reducing L/D.

It came as a surprise that distinct eye-like patterns could not be found near closed free ends, even at a length-to-diameter ratio as high as 10. Some confusing localized three-dimensional flow patterns were found at different locations along the span. They appeared randomly and asymmetrically relative to both the x- and y-axes of symmetry of the cylinder. Figure 7 shows the typical appearance of these patterns, two on the top and three on the bottom surface. Note that separation lines remained straight, unlike the Gould *et al.* (1968) eye-like pattern (see figure 1).

The same surface patterns with finer details are shown in figure 8 for $L/D = 5$. The surface skin-friction lines indicate some sort of weak swirling flow. When the length-to-diameter ratio was shortened below 4, the separation line started to bow as seen

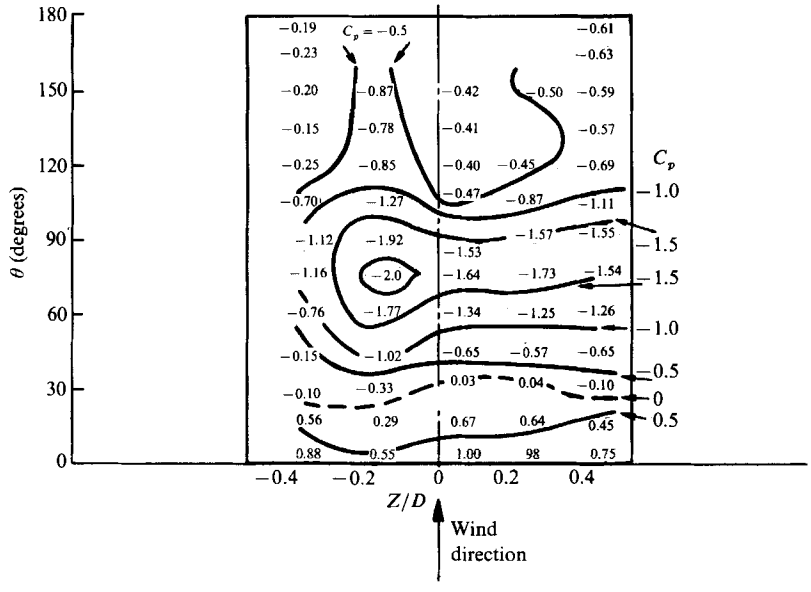

FIGURE 10. Isobars for $L/D = 1$ on an unwrapped half-cylinder. $Re = 2.55 \times 10^5$.

in figure 9 for $L/D = 2$. The minimum angle of separation did not occur in the plane of symmetry and the bow appeared displaced for $-0.15D$ to the left. It suggests that the overall flow is also asymmetric. These unexpected features prompted the subsequent pressure measurements to be taken on the left- and right-hand sides of the model simultaneously.

6. Spanwise pressure distribution

The pressure measurements around the circumference and along the span of the model are carried out only on the 127 mm model. All pressure tappings are located on the upper side of the cylinder ($0 \leqslant \theta \leqslant 180°$). Only the pressure tappings on five rings can be connected to a multimanometer during one run. This means that simultaneous measurements of all available tappings are possible only on the shortest model of $L/D = 1$.

Figures 10 and 11 show two ways of presenting pressure distributions. Figure 10 shows half of the unwrapped circumference with measured values of pressure coefficients, $C_p = (p - p_0)/q_0$ where p is the static pressure, along five rings of tappings. The estimated isobars are drawn between the measured points. A remarkable feature is the distinct asymmetry of isobars. The minimum value of the pressure coefficient (-2.01) is displaced $-0.2D$ from the plane of symmetry.

Figure 11 shows the conventional presentation of pressure distributions around five rings. The broken curve shows the pressure distribution around an infinite cylinder. The minimum pressure coefficient, $C_{p\min}$, is around 60° and separation is around 80°. However, for the finite cylinders, $C_{p\min}$, occurs at around 80° and the separation point is displaced to around 100° judging by the inflection of the adverse pressure gradient. There is a considerable difference in the measured base pressure coefficient at $\pm 0.4D$, which produces a yawing moment. The minimum pressure near 80° is also displaced away from the plane of symmetry, which produces a rolling

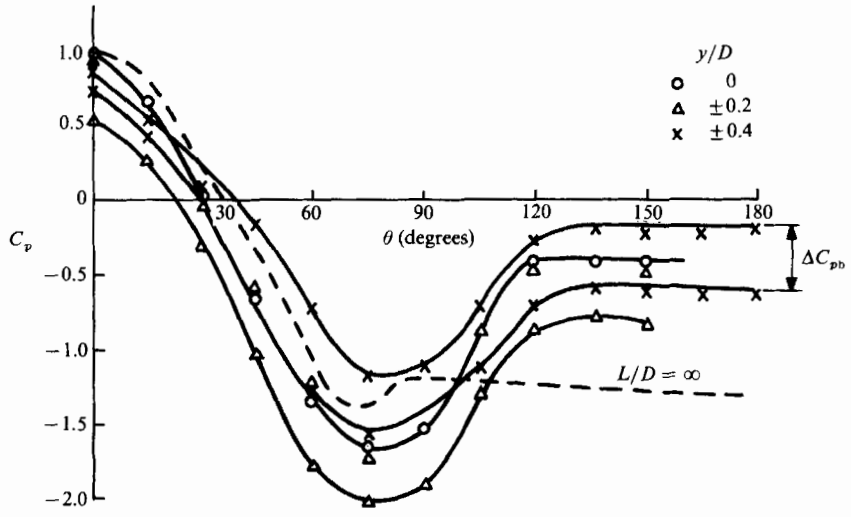

FIGURE 11. Pressure distributions for $L/D = 1$ (conventional). $Re = 2.55 \times 10^5$.

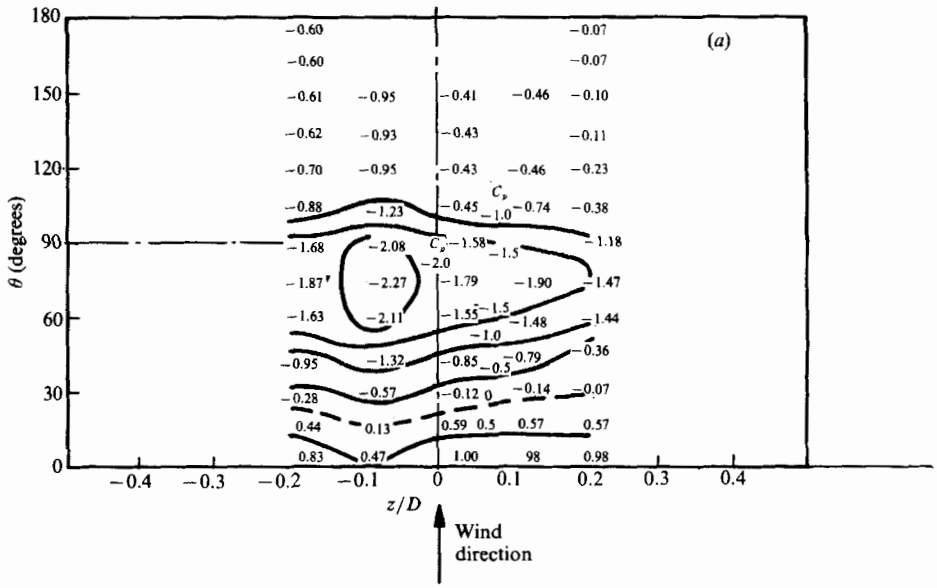

FIGURE 12(a). For caption see facing page.

moment. When the model was extended to $L/D = 1.5$ by inserting two more rings, the pressure distribution was asymmetrical and the isobar pattern was similar to that shown in figures 10 and 11.

The model was further extended to $L/D = 2$ by inserting two more rings with pressure tappings. Only the pressure tappings from five rings could be connected to the multimanometer and three runs were necessary to cover the whole model. Figure 12(*a–c*) shows an incomplete isobar pattern with various rings connected and disconnected. The typical asymmetric isobar pattern seen in figure 12(*a*) is similar to that in figure 10 and the minimum pressure is on the left-hand side. The minimum

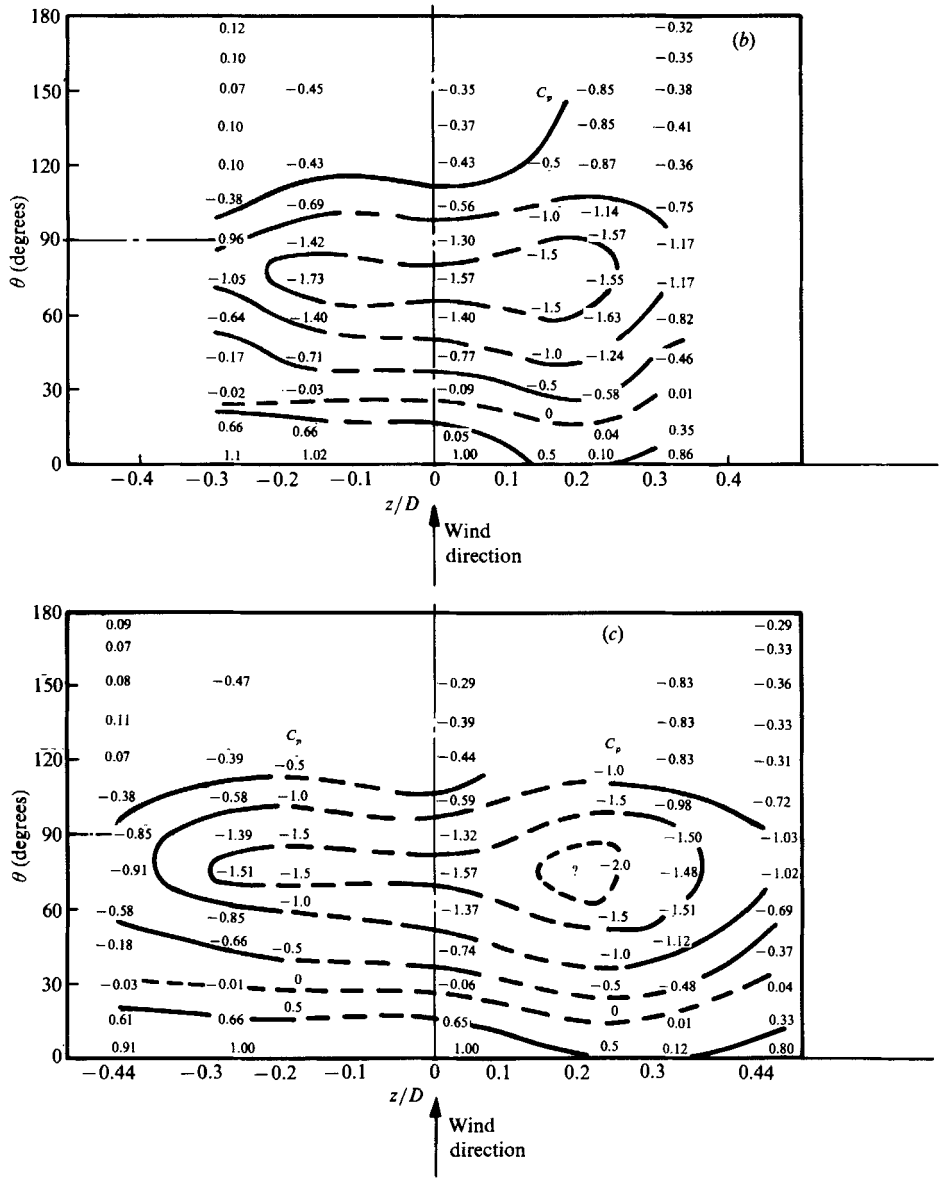

FIGURE 12. Isobars for L/D = 2.0, without some rings: (*a*) ±3 and ±4, (*b*) ±1 and ±4, (*c*) ±1 and ±2. $Re = 2.6 \times 10^5$.

pressure switched to the right-hand side in subsequent runs shown in figure 12(*b*, *c*). It appeared that the asymmetry is bistable and can be biased to either side of the cylinder.

Some qualitative tests were carried out in order to establish the effect of yaw angle of the model on the observed asymmetry. The model was slowly yawed over a range of ±15° to the *z*-axis. Yaw angles greater than 2° enhance the asymmetry on the corresponding side of the model. It is noted that the asymmetry on one side possesses some stability in that the switch to the other side occurs with a hysteresis lag of up to 3°. From these preliminary tests it appeared that asymmetric flow regimes are

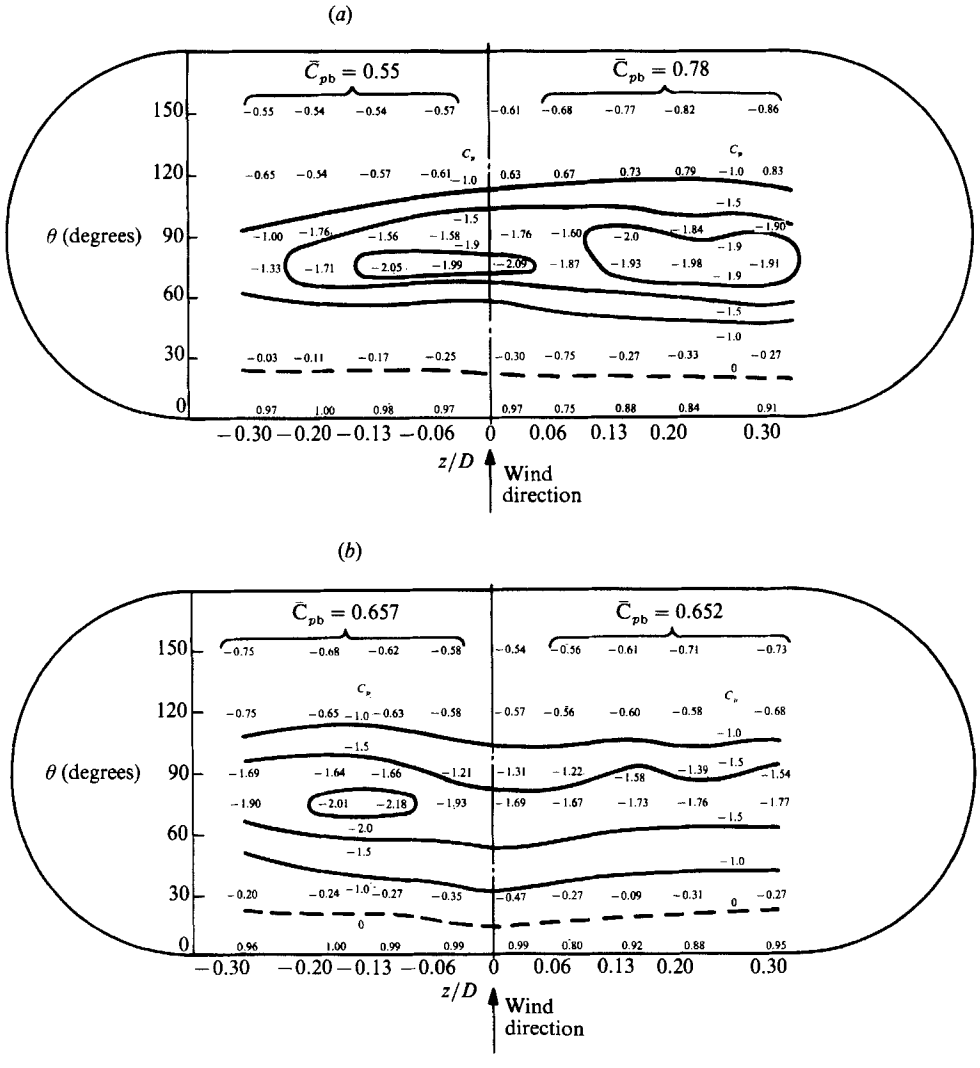

FIGURE 13. Isobars for $L/D = 3$ and hemispherical ends. (*a*) $Re = 2.2 \times 10^5$, (*b*) $Re = 2.6 \times 10^5$ (Note that hemispherical ends should be elliptic when unwrapped, not circular as shown).

stable for yawed cylinders and bistable for the small and zero-yaw angles. The symmetric flow pattern is not found because it is presumably intrinsically unstable as in the flow behind two side-by-side cylinders at close spacing (Zdravkovich 1977).

The possible effect of the mounting system was also checked. The mounting system and model were arranged so that the free stream first reached the mounting system and then the model. The effect of this reversed arrangement was found to be insignificant on the measured pressure distribution and the asymmetry was not affected.

Another possible cause for the asymmetry might be an unequal entrainment into the near wake around the two flat free ends. If so, then the rounded free ends might reduce the asymmetry. In order to check this hypothesis, the flat free ends were replaced by two hemispherical caps. This extended the length-to-diameter ratio to 3.

Run	$Re \times 10^5$	$\bar{C}_{pbl}$	$\bar{C}_{pbr}$	$\Delta\bar{C}_{pb}$
65	2.16	0.762	0.572	0.19
63	2.21	0.55	0.78	0.23
66	2.34	0.568	0.746	0.18
64	2.60	0.657	0.652	0.005

C_{pbl} is mean spanwise base pressure on the left-hand side, and C_{pbr} that on the right.

TABLE 1. Average base pressure on two sides of the hemispherical cylinder, $L/D = 3$

The number of monitored pressure tappings per ring was halved in order to obtain simultaneous pressure measurements of all nine rings. Figure 13(*a*) shows a significant asymmetry; for example, the average base pressure coefficients are different on two sides. However, there was some kind of transition to a more symmetric flow regime which occurred beyond $Re = 2.4 \times 10^5$. Table 1 shows the summary for four runs and figure 13(*b*) shows the isobar pattern of the 'symmetric' flow regime. Note that the difference in the minimum pressure coefficient is enhanced in the latter case. It seems that the shape of free ends does not affect asymmetry, at least for $Re < 2.5 \times 10^5$.

7. Measurements of yawing and rolling moments

The observed asymmetry of pressure distribution relative to the plane of symmetry of the model produces a rolling moment around axis x (along the free stream) and a yawing moment around axis y (normal to the free stream and the length of the model). Both moments are affected not only by the magnitude of the uneven pressure distribution but also by the distance of the resulting pressure force from the axis of symmetry. Hence it is expected that the similar asymmetry will induce decreasing moments for shorter models.

Unlike the drag force, the magnitude of which is in the middle range of the balance, the yawing and rolling moments are found to be much smaller but still measurable. The readings fluctuated by $\pm 50\%$ and $\pm 80\%$ about a mean non-zero value for the yawing and rolling moment, respectively. The models tested have $L/D = 2$, 4, 6 and 8, all of 89 mm diameter.

Figure 14 shows the erratic variation of the coefficient of yawing moment, $C_y = M_y/qLD^2$ where M_y is the yawing moment, with Reynolds number for four length-to-diameter ratios. For all models the expected change of sign of the yawing moment is evident except for $L/D = 4$. Some drift and hysteresis of data for $L/D = 6$ are also included in figure 14. The scatter of experimental points is mostly caused by the inadequacy of the balance and the values of C_y should be taken cautiously.

Figure 15 shows the erratic variation of the coefficient of rolling moment $C_r = M_r/qLD^2$, with Reynolds number for the four models tested. The change of sign occurs only for two models and the scatter of experimental points is similar to that in figure 14. The dashed lines denote five possible flow regimes for $L/D = 2$. The comparison of C_y and C_r graphs does not show any correlation. These measurements are presented rather as a qualitative support to pressure measurements than a quantitative data base.

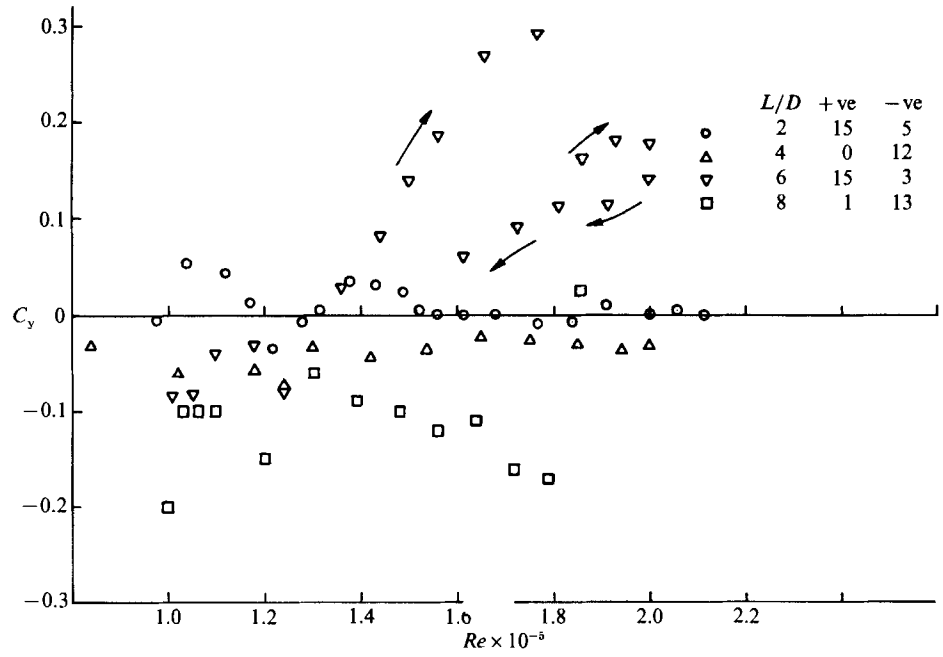

FIGURE 14. Yawing moment versus Reynolds number; the number positive of and negative readings are listed.

8. Vortex shedding

Vortex shedding behind a cylinder with two free ends is of fundamental and practical importance although neither Wieselsberger (1922) nor subsequent researchers measured the frequency of vortex shedding. Okamoto & Yagita (1973) proposed that the flow around a finite circular cylinder with one free end mirrors itself in the plane boundary and, if so, it is analogous to flow around a cylinder with two free ends of a double H/D value. The vortex shedding does not occur for the former for $H/D < 5$ or 6, and this should also be the case for $L/D < 10$ for the cylinder with two free ends.

It came as a surprise that vortex shedding existed at $z/D = 0$ behind all four tested cylinders, $L/D = 2$, 4, 6 and 8. Admittedly, it was more irregular and the frequency peak was wider than behind a cylinder of infinte span. The signal was occasionally periodic with very little modulation, then it was interrupted by irregular periods to be succeeded by another set of periodic signals with a visibly different frequency than before. The variation in frequency made it impossible to assign a single value for the Strouhal number; instead, the measurements are presented in figure 16 with vertical bars and two solid and dotted curves for the extreme Reynolds numbers. A correlation of signals from two hot wires located on the opposite side of the near wake was only observed but not pursued further.

Figure 16 shows the vortex shedding frequency measured by a hot wire located $x/D = 1.7$, $y/D = 0.7$ and $z/D = 0$. The three Reynolds numbers correspond to the near minimum, medium and maximum obtainable velocity in the wind tunnel. The width of the frequency band seems to increase as the length-to-diameter ratio decreases and the mean value of Strouhal number shows an increase for $L/D = 2$. The latter trend is hard to explain, because it suggests that the wake width decreases,

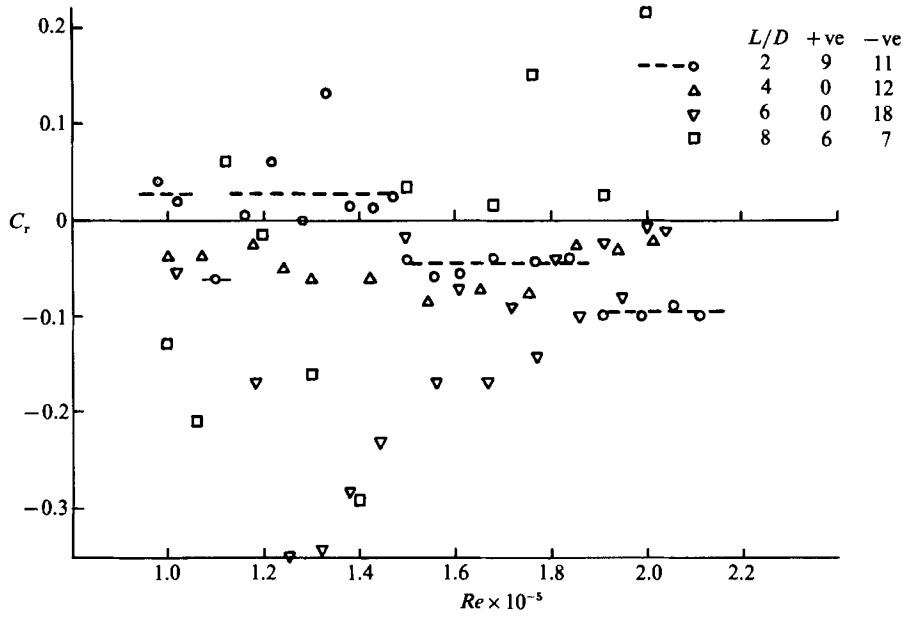

FIGURE 15. Rolling moment versus Reynolds number; the number of positive and negative readings are listed.

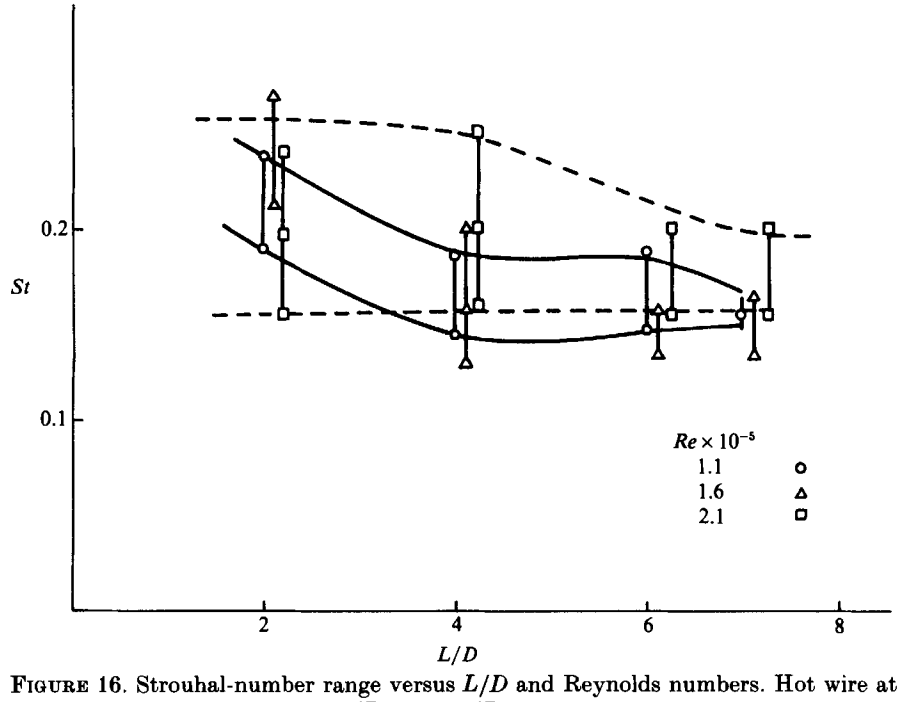

FIGURE 16. Strouhal-number range versus L/D and Reynolds numbers. Hot wire at $x/D = 1.7$, $y/D = 0.7$.

which apparently does not affect the drag coefficient. It seems that the concept of a universal Strouhal number breaks down for the finite cylinders where three-dimensional flow dominates.

Similar observations were made by Ayoub & Karamcheti (1982) who measured the frequency of vortex shedding near the free end of a circular cylinder of $H/D = 12$ at

$Re = 7.7 \times 10^5$. They stated that the vortex shedding in the tip region was distinct from that prevailing on the main body of the cylinder. In particular the tip vortex shedding can be unstable and intermittent. This description fits the present observations except that there was no 'main body vortex shedding' because the hot wire was placed in the plane of symmetry.

9. Closing comments

The effects of two free ends on the flow around short cylinders have raised many questions which would lend themselves to further study;

(i) The rate of fall of drag coefficient diminishes with reducing L/D and becomes negligible for $L/D < 6$. This might indicate two flow regimes: (*a*) The inflow behind the free ends becomes gradually less effective as L/D decreases from ∞ to 6. (*b*) The inflow behind short cylinders, $L/D < 6$, cannot reduce the drag any further became the drag is governed by the shape of the free ends. When hemispherical ends are used, the drag is further reduced until $L/D = 1$, at which the cylinder with hemispherical ends becomes a sphere. However, for the flat-ended cylinders the limit is $L/D \to 0$ which is not investigated.

(ii) The Reynolds-number effect is similar to that found on a cylinder of infinite length. However, the separation lines are displaced gradually towards the stagnation line as L/D decreases and eventually become bow-shaped for $L/D = 2$.

(iii) The vortex shedding does not cease on decreasing L/D down to 2. It is irregular, spreads over a wider frequency band and interrupts intermittently. The Strouhal number is in the range of 0.14 to 0.25. The evidence suggests that when vortex shedding occurs, it does so at one single frequency, but that frequency is not the same at different times of shedding. The concept of a universal Strouhal number, which is established on the basis of data taken with infinite cylinders, cannot be used in regions of highly three-dimensional flow such as near the ends of a finite cylinder.

(iv) The flow around very short cylinders is found to be asymmetric in respect of the plane of symmetry of the cylinder. An uneven base pressure behind the two halves of the cylinder is found for both flat-ended and hemispherically ended cylinders. The asymmetry is bistable and hysteretic, i.e. the location of minimum pressure can change over from one side of the cylinder to the other. The resulting yawing and rolling moments are small.

REFERENCES

AYOUB, A. & KARAMCHETI, K. 1982 An experiment on the flow past a finite circular cylinder at high subcritical and supercritical Reynolds numbers. *J. Fluid Mech.* **118**, 1–26.

ETZOLD, F. & FIEDLER, H. 1976 The near-wake structure of a cantilevered cylinder in cross flow. *Z. Flugwiss.* **24**, 77–82 (in English).

FARIVAR, D. J. 1981 Turbulent uniform flow around cylinders of finite length. *AIAA J.* **19**, 275–281.

GOULD, R., RAYMER, W. G. & PONSFORD, P. J. 1968 Wind tunnel tests on chimneys of circular cross section at high Reynolds number. *Proc Symp Wind Effects on Buildings and Structures, Loughborough* (ed. D. J. Johns), Vol. 2, Paper 10.

KAWAMURA, T., HIWADA, M., HIBINO, T., MABUCHI, I. & KUMADA, M. 1984*a* Flow around a finite circular cylinder on a flat plate. *Bull. JSME* **27**, 2142–2151.

KAWAMURA, T., HIWADA, M., HIBINO, T., MABUCHI, I. & KUMADA, M. 1984*b* Heat transfer from a finite circular cylinder on the flat plate. *Bull. JSME* **27**, 2430–2439.

MUTTRAY, H. 1932 The experimental facts of drag without lift. *Handbuch der Experimentalphysik*, Vol. 4.2 (ed. L. Schiller), 521, pp. 318–321. Berlin (in German).

OKAMOTO, T. & YAGITA, M. 1973 The experimental investigation on the flow past a circular cylinder of finite length placed normal to the plane surface in a uniform stream. *Bull. JSME* **16**, 805–814.

SAKAMOTO, H. & ARIE, M. 1983 Vortex shedding from a rectangular prism and a circular cylinder placed vertically in a turbulent boundary layer. *J. Fluid Mech.* **126**, 147–165.

SLAOUTI, A. & GERRARD, J. H. 1981 An experimental investigation of the end effects on the wake of a circular cylinder towed through water at low Reynolds number. *J. Fluid Mech.* **112**, 297–314.

TANEDA, S. 1952 Studies on wake vortices. *Rep* 1, *Research Institute of Applied Mechanics, Kyu-Shu University*, Vol 1, No 4, pp. 131–143.

WIESELSBERGER, C. 1982 On the drag of circular cylinders. *Phys. Z.* **23**, 219–224 (in German).

ZDRAVKOVICH, M. M. 1977 Review of flow interference between two circular cylinders in various arrangements. *Trans ASME* I: *J Fluids Engng* **99**, 618–633.

ZDRAVKOVICH, M. M. 1983 Flow around two circular cylinders forming a cross. *J. Fluid Mech.* **128**, 231–246.

ZDRAVKOVICH, M. M. 1988 Conceptual overview of laminar and turbulent flows past smooth and rough circular cylinders. *Proc. Intl Colloq. on Bluff Body Aerodynamics and Its Applications, J. Wind Engng* (*Japan Assoc Wind Engng*), *Tokyo*, No 37, pp. 93–102.